RAPID COMMUNICATION

Quantitative analysis of the morphing wing mechanism of raptors: Morphing kinematics of *Falco peregrinus* wing

Di Tang(唐迪)[1,†], Jinqi Che(车婧琦)[1], Weijie Jin(金伟杰)[1], Yahui Cui(崔亚辉)[2], Zhongyong Fan(范忠勇)[3], Yin Yang(杨茵)[4], and Dawei Liu(刘大伟)[4]

[1] *College of Mechanical Engineering, Zhejiang University of Technology, Hangzhou* 310014, *China*
[2] *Affiliated HangZhou XiXi Hospital, Zhejiang University School of Medicine, Hangzhou* 310023, *China*
[3] *Zhejiang Museum of Natural History, Hangzhou* 310014, *China*
[4] *High Speed Aerodynamic Institute, China Aerodynamics Research and Development Center, Mianyang* 621000, *China*

(Received 16 August 2022; revised manuscript received 19 October 2022; accepted manuscript online 11 November 2022)

Raptors are getting more attention from researchers because of their excellent flight abilities. And the excellent wing morphing ability is critical for raptors to achieve high maneuvering flight, which can be a good bionic inspiration for unmanned aerial vehicles (UAV) design. However, morphing wing motions of *Falco peregrinus* with multi postures cannot be consulted since such a motion database was nonexistent. This study aimed to provide data reference for future research in wing morphing kinetics. We used the computed tomography (CT) approach to obtain nine critical postures of the *Falco peregrinus* wing skeleton, followed with motion analysis of each joint and bone. Based on the obtained motion database, a six-bar kinematic model was proposed to regenerate wing motions with a high fidelity.

Keywords: raptor, wing morphing, skeletal mechanism, CT scans, six-bar model

PACS: 47.32.cd, 47.32.Ff **DOI:** 10.1088/1674-1056/aca201

1. Introduction

Unlike modern aircraft, birds can actively morph their wings to accomplish extraordinary flight.[1–3] They can actively change speed and direction, complete cruising, soaring, turning, landing, diving, and other incredible motions.[4–7] Shatkovska[8] found that birds with different wing morphology have different flight patterns. Liu *et al.*[9] conducted a 3D scanning of the wing geometry of several birds and established a flapping avian wing model with correct kinematics. Raptors' maneuvering flight is often used for aerial hunting and pursuit.[10] Robin *et al.*[11] simulated the high-altitude diving, wing flapping, and gliding of *Falco peregrinus* through a 3D modeling approach, and confirmed that high-altitude diving can obtain powerful aerodynamic force, which is conducive to capturing aerial prey. Lewis *et al.*[12] measured the flight variables of three raptors using accelerometer data loggers, which provided information for the comparative analysis of bird behaviors and energetics. Understanding avian wing morphing inspires the control of novel UAVs.[1]

Almost all birds can change the shape of their wings during the flight to change their aerodynamic characteristics, which is known as the concept of wing morphing.[6] *Falco peregrinus* also change the shape of their wings when diving, wings will get closer to the body while accelerating.[13] The flight of *Falco peregrinus* can be divided into three stages: the wings are in the classic diamond shape at a speed up to 190 km/h. At 240 km/h, the wings show a tight vertical tuck and have a cupped-like profile in the front. At the maximum speed (at least 320 km/h), the wings are completely folded on both sides of the body to form a wrap dive vacuum pack.[14] *Falco peregrinus* can achieve high-speed and high-maneuver flight at the same time, which indicates that they are exposed to high mechanical loads. For example, in courtship behavior, they often change their flight path at the end of the dive, i.e., from vertical dive to steep climb.[15]

The basis of wing morphing is the musculoskeletal mechanism, which was first recorded in Bergman's anatomical study of cadavers in 1839.[16] This mechanism is regarded as a parallelogram four-bar mechanism that can automatically flex and extend[17,18] since bird wings have a special skeletal structure. The elbow joint connects the humerus, radius, and ulna while the wrist joint connects the ulna, radius and carpometacarpus, as shown in Fig. 1. Fisher[19] confirmed the elbow–wrist joint coupling mechanism through anatomical experiments on pigeons in 1957. Furthermore, the elbow–wrist joint coupling motion is essential in bird flight. It will lead to difficulty in flight if the bird lacks control of the radius and ulna due to injury. A Mississippi kit was wound with a bandage due to the fracture of the ulna, resulting in the fusion of the ulna and radius, and losing the ability to extend wings and fly. It recovered only after the ulna and radius were separated by surgery.[20] Similarly, a barn owl was amputated due to a serious injury of the radius. It was unable to control its wings stably and lost its wing extension and flight ability.[21]

[†]Corresponding author. E-mail: tangdi@zjut.edu.cn

© 2023 Chinese Physical Society and IOP Publishing Ltd

In 1994, Vazquez[22] found that except for the wing skeleton, the special attachment of the muscles and tendons of the wings also affected the elbow–wrist joint coupling motion. David[23] confirmed this muscle and ligament mechanism through computed tomography and anatomical experiments on pigeons. In 2005, Meyers *et al.*[24] performed an anatomical and immunohistochemical evaluation of the albatross and found that the albatross uses slow muscle fibers and rigid restrictive tendons to maintain a long-term sliding posture. By comparing the permutation of the ulna and radius of birds with other vertebrates, researchers found that the parallel permutation of the radius and ulna of birds coordinated the elbow–wrist joint coupling motion. Birds can achieve wing morphing more flexibly than other flying vertebrates, and make efficient use of aerodynamic force to complete the flight.[25] Understanding the permutation of the ulna and radius provides an extremely useful understanding of the flight patterns of birds.[26]

However, many studies on the kinematic model of bird wings regard the wing skeleton as a planar four-bar mechanism, ignoring the effect of wrist bones on the flight;[27,28] or consider the ulna and radius as a single bone, and the wing is an open-loop kinematic system starting from the shoulder joint.[23,29] Vazquez[30] found for the first time in an anatomical experiment that wrist bones can also move and coordinate wing morphing during the flight. Therefore, the real physiological state of the skeleton should be fully considered when studying the kinematic characteristics. In 2007, Amanda[25] further studied the mechanical linkage of the musculoskeletal structure of pigeon wings and analyzed the flexed and extended posture quantitatively through μCT data and the least square mathematical method. It was found that the wing skeleton is a three-dimensional mechanism, and the radial and ulnare can't be ignored. Finally, a six-bar model with 8 DOFs was established, as shown in Fig. 1.

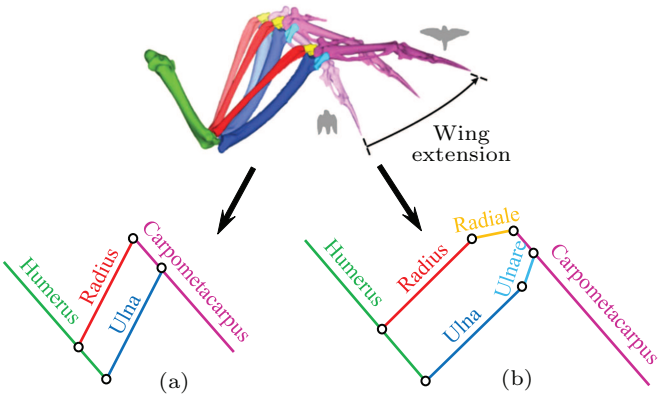


Fig. 1. Parallelogram mechanism of wing skeleton: (a) four-bar model,[22] (b) six-bar model.[25]

Bionic technology has been widely used in UAVs. The primary methods include numerical analysis, modeling, simulation, machine design, etc.[31–33] Biologically inspired mechanical linkage can accomplish complex maneuvers and optimize force and motion, which is very common in bionic UAVs.[34–36] Zhang *et al.*[37] designed a single-DOF planar linkage bionic mechanism. The positions of all reference points were continuously constrained by the constraint descent method to meet the requirements of the bionic mechanism in shape, motion trajectory and posture. Rajabi *et al.*[38] accomplished the interlocking mechanism of dragonfly wing joints using unidirectional hinges. Although investigations on the coordination function of the musculoskeletal structure of bird wings have continued for decades, there are still some deficiencies remained, especially for raptors. Falconidae has contrasting behaviors in flight within the subfamilies. *Falco peregrinus* is an aerial predator requiring accuracy, high-speed, and controlled-motion during flight. They are famed for their high-speed and high-altitude stoops. *Falco peregrinus* has probably the fastest hunting speed among all birds, so it has high physiological research value.[11] These extraordinary maneuvers are intimately related to their biomechanical constraints. We established the *Falco peregrinus*'s wing model using guidance laws inspired by theory and experiment, attempted to find out the mechanism of *Falco peregrinus*'s superior flight performance and embody this in the field of bionic UAVs design to improve the mobility and flexibility.

The wing morphing of the existing ornithopter is flapping, and large angles and multiple DOFs mainly occur at the shoulder joint, which is a connection between the wing and the fuselage. This paper mainly studies the elbow–wrist joint coupling motion, i.e., the closed-loop mechanism in complex motion with multiple DOFs, to improve the flexibility of wing morphing of bionic UAVs. Little research has been conducted on wing morphing with large angles and multiple DOFs, and there is a need for studying various wing postures. Moreover, a few joints show obvious single DOF characteristics during motion, and reducing the DOFs as much as possible can make the control easier. Therefore, to fill this gap in the avian literature, this paper studies the kinematic characteristics of the *Falco peregrinus* wing and attempts to reduce the redundant DOFs of the kinematic model based on the spherical joint. Using established joint optimization techniques, we proposed a kinematic model that meets the requirements of various postures of the *Falco peregrinus* wing.

2. Material and methods

Falco peregrinus is one of the world's fastest birds, reaching speeds of 320 km/h before striking its prey.[15] Investigation of *Falco peregrinus* wing would be well suited for future quantitative studies about avian flights. To obtain the musculoskeletal information of *Falco peregrinus* forelimb, we cooperated with Zhejiang Museum of Natural History to obtain a

specimen of an abnormally dead *Falco peregrinus*. The frame was composed of carbon-fiber pipes. Two adjacent carbon-fiber pipes were connected by T-branch pipes or four-way pipes made of low-density plastic. A testbed was built in the middle to support the body. Each wing was fixed on the carbon-fiber pipes with two pairs of nylon wires and fasteners. Nine critical postures of the wing were suspended and fixed by moving the position of the fasteners on the carbon-fiber pipes and adjusting the length of the nylon wires, as shown in Fig. 2(a).

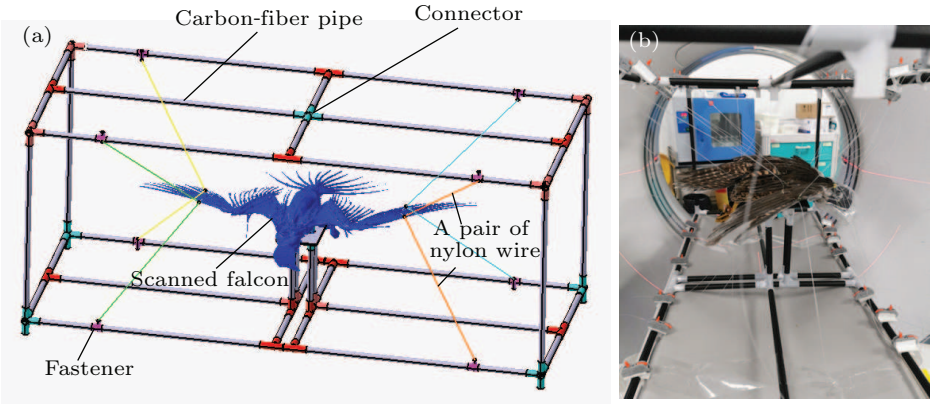


Fig. 2. Suspension and fixing system for CT scanning experiment of *Falco peregrinus* wing.[39]

As a result, a bird suspension system was established. Before the CT scans, the carcass was placed and adjusted to a flight pose, followed by the fastening of all nylon wires, as shown in Fig. 2(b). Each nylon wire was tightened so that each wing could maintain its geometric shape during the entire scanning test. The carcass shapes were manually adjusted to particular flight postures according to the flight photos provided by ornithologists of Zhongyong Fan's team, because the dead *Falco Peregrinus* could not move its wings naturally. Thereafter, we cooperated with the Cui's team of affiliated Hangzhou XiXi Hospital, and CT scanning experiment was performed on the entire body of *Falco peregrinus* specimen. Subsequently, a clinical scanner was used to obtain the plain CT image with a slice thickness of 0.625 mm, and the skeleton model of *Falco peregrinus* wing was reconstructed through the CT imaging to obtain the scanned bones with different postures. A total of nine critical postures of the wing were obtained: extension, half flexion, flexion, small torsion, large torsion, small deep stall, large deep stall, flap down and flap up.

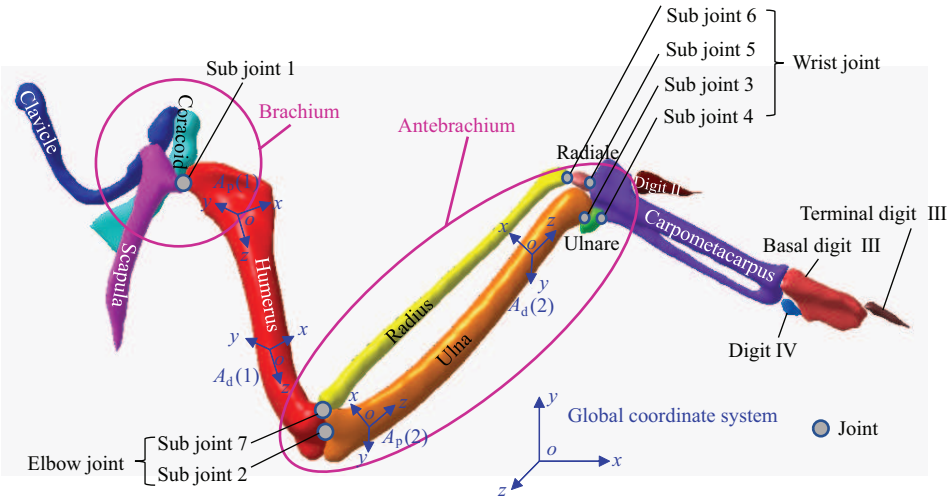


Fig. 3. Bones, joints and coordinate systems of the right forelimb of *Falco peregrinus*.

The forelimb skeleton was divided into two main parts. The brachium was composed of scapula, coracoid, clavicle and humerus; and the antebrachium was composed of humerus, ulna, ulnare, carpometacarpus, radiale and radius. In order to analyze the kinematics of the wing quantitatively, the nine postures (extension, half flexion, flexion, small torsion, large torsion, small deep stall, large deep stall, flap down and flap up) were marked as $j = 1$ to 9 in sequence. The scanned antebrachium bones (humerus, ulna, ulnare, carpometacarpus, radiale and radius) were marked in counterclockwise order as

$i = 1$ to 6 to form a closed-loop mechanism with six bars. The corresponding joints were marked in counterclockwise order as $k = 1$ to 7, as shown in Fig. 3. Joint 1 was the shoulder joint, joints 2 and 7 formed the elbow joint, and joints 3, 4, 5 and 6 formed the wrist joint. Since each bone rotated during wing morphing, a local coordinate system was established to describe motions of bones, as shown in Fig. 3. Rigid body motions, joint connections were described using these moving frames. Here, only the local coordinate systems of the proximal and distal end of bone 1 (humerus) and bone 2 (ulna) were presented. Bones, joints and coordinate systems of the right forelimb of the *Falco peregrinus* were the main components of the wing skeleton model.

Wing motions were quantitatively measured based on the CT data using the proposed optimization algorithm, in detail, translations, rotating axes and rotating angles of each bone were obtained. Thereafter, translations and rotations from one posture (the extended posture, in the current study) to the other postures can be obtained by a simple calculation. Filter the bone points on the premise of ensuring fitting precision. The point numbers of the humerus, ulna, radius and carpometacarpus were 1672, 1238, 644 and 785, respectively. Ulnare and radiale were composed of 532 and 424 points. The averaged minimum distance optimized by the algorithm was defined as the residual value to evaluate the degree of bone fitting.

3. Quantitative measurement of wing joint motions

3.1. Measure method

The fixed bone was regarded as parent bone and the moving one was regarded as child bone in each joint. The parent bones of all postures were fitted and fixed at the same position. We corroborated kinematic characteristics based on the CT data using a proposed optimization algorithm. No constrained equations were used in the algorithm in consideration that each bone may move in a 6 DOFs manner in nature wing morphing. Translations, rotating angles and axes for each child bone were optimized to guarantee the best-fit bone position, where a minimum residual was achieved. Therefore, the unconstrained residual can be taken as the evaluation criteria of six-bar closed-loop mechanism in the following analysis.

Order wing posture with j and bone with i. The translation variable T_i and rotation variable R_i were used to represent the position of the bone i in the extended posture in the global coordinate system. The current location $L_{i,\mathrm{curr}}$ of moved bone i can be calculated using the following equation:

$$L_{i,\mathrm{curr}} = R_i L_{i,\mathrm{init}} + T_i, \tag{1}$$

where $L_{i,\mathrm{init}}$ is the location of bone i in the initial extended posture. Thereafter, the average distance between the moved bone i in the extended current posture and the one in the posture j can be calculated as

$$d_{ij} = \frac{1}{N_{ij}} \sum_{m=1}^{N_{ij}} \sqrt{(L^m_{ij,\mathrm{init}} - L^n_{i,\mathrm{curr}})^2}, \tag{2}$$

where N_{ij} denoted the point number of the cloud of bone i in posture j, N_i denoted the point number of the cloud of bone i in extended posture. A loop was used to find the minimum value between point $L^m_{ij,\mathrm{init}}$ and $L^n_{i,\mathrm{curr}}$. Finally, the following global optimization equation, using the GlobalSearch method in MATLAB software, was used to find the minimum residual:

$$f(R_i, T_i) = \min(d_{ij}), \tag{3}$$

where R_i and T_i were optimization variables with no constraints.

3.2. Results and discussion

The motions (both axis and angle) including humerus relative to the scapula, radius and ulna relative to the humerus, ulnare relative to the ulna, radiale relative to the radius, carpometacarpus relative to the ulna were measured by a step-by-step point cloud fitting approach,[39] as shown in Figs. 4(a)–4(f). The red bone represented the one in the extended posture. Firstly, it rotated around the rotating axis to the middle posture (the orange one), and then translated to reach the target posture (the yellow one).

The pectoral girdle was composed of scapula, coracoid and clavicle. Three main bones formed a glenoid to construct the shoulder joint with humerus, as shown in Fig. 3. Therefore, these three bone motions were used to study the shoulder joint behaviors. During the quantitively analysis, the extended posture was identified as the reference frame, parent bones (scapula) of all the other eight postures were transformed to the same position at first, as shown in Fig. 5(a). Thereafter, motions (both translations and rotations) of coracoid relative to the scapula, humerus relative to the scapula were calculated to obtain relative displacement, rotating axes and rotating angles as listed in Table 1. It was shown that the translations of coracoid relative to scapula were within 1 mm, meanwhile, the maximum rotating angle was under 6.4°, which appeared in the large deep stall posture. Motion of the coracoid relative to the scapula was negligible during normal flight. Therefore, coracoid individual motion was not considered in the current study.

On the other hand, the maximum translation of humerus was 2.558 mm in the large deep stall case, and the translations of other postures were all within 2 mm. A maximum rotating angle of 27° was observed in the large torsion case. Rotating angle of the flexed posture was nearly twice the one of half flexed posture, which were 21.255° and 11.661°, respectively. The angles of flap down and flap up were closed, which

were 25.958° and 21.937°, respectively, but in opposite directions. Translations and rotations indicate that relative move of humerus to scapula (coracoid) constituted the shoulder joint function.

As a result, the motion of the shoulder joint was further simplified: the scapula and coracoid were regarded as one rigid body to represent the *Falco peregrinus* body, and the motion of the shoulder joint was represented by the motion of the humerus relative to the scapula. The shoulder joint was found to be essential to wing morphing motions, which can help the wings to accomplish various critical postures.

The elbow joint was composed of the humeroulnar joint and humeroradial joint, where the motions of ulna relative to humerus, radius relative to humerus were quantitively measured as listed in Table 2. It was shown that translations of all the postures were within 1.5 mm which was so small that they can be ignored. The rotating angle of flexed posture was about twice as the one of half flexed posture, which were 38.8941° and 16.1220°, respectively. The small angle of the ulna indicated the ulna played a small role in flap up and torsion motions. The direction of the two joints rotating axes covered x, y, and z directions. Rotating in all directions with neglectable relative translations indicated the elbow acted more like a spherical joint.

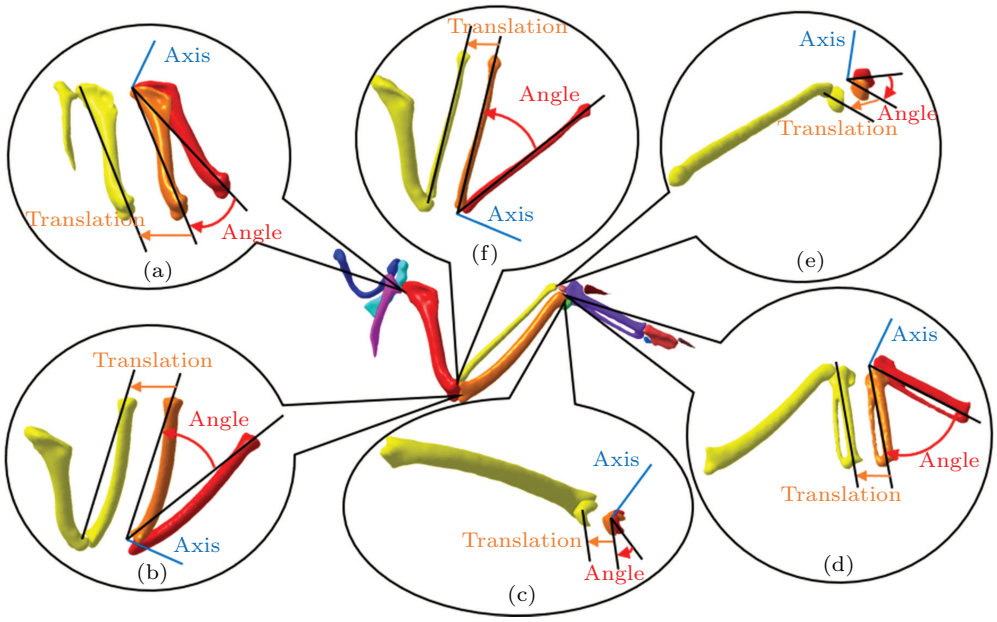


Fig. 4. Rotation and translation steps of each moving bone: (a) humerus; (b) ulna; (c) radius; (d) ulnare; (e) radiale; (f) carpometacarpus.

Table 1. Relative motion of the shoulder joint.

Posture	Coracoid relative to scapula					Humerus relative to scapula				
	T (mm)		A		θ (°)	T (mm)		A		θ (°)
Half flexion	0.267	0.267	0.267	0.267	0.267	0.660	0.586	–0.037	–0.810	11.661
Flexion	0.750	0.750	0.750	0.750	0.750	1.746	–0.018	0.067	–0.998	21.255
Small torsion	0.747	0.747	0.747	0.747	0.747	1.713	–0.413	0.888	0.201	20.696
Large torsion	0.616	0.616	0.616	0.616	0.616	1.435	–0.503	0.825	0.258	27.030
Small deep stall	0.804	0.804	0.804	0.804	0.804	1.925	0.173	–0.841	0.514	12.747
Large deep stall	0.860	0.860	0.860	0.860	0.860	2.701	–0.055	–0.975	0.216	19.420
Flap down	0.404	0.404	0.404	0.404	0.404	1.651	–0.947	–0.196	0.256	25.958
Flap up	0.543	0.543	0.543	0.543	0.543	0.447	0.829	0.276	–0.486	21.937

Table 2. Relative motion of the elbow joint.

Posture	Ulna relative to humerus					Radius relative to humerus				
	T (mm)		A		θ (°)	T (mm)		A		θ (°)
Half flexion	0.356	–0.129	–0.146	0.981	16.122	0.642	–0.460	–0.422	0.781	20.617
Flexion	1.085	–0.266	–0.128	0.956	38.894	1.273	–0.287	–0.191	0.939	38.838
Small torsion	0.171	–0.064	0.858	–0.510	4.538	0.354	–0.387	0.753	–0.532	4.437
Large torsion	0.469	0.038	0.653	–0.756	8.432	0.726	–0.356	0.384	–0.852	7.762
Small deep stall	0.315	0.380	–0.458	–0.803	14.813	0.844	0.242	–0.603	–0.761	15.309
Large deep stall	0.260	0.488	–0.431	–0.759	11.663	0.474	–0.094	–0.862	–0.498	15.899
Flap down	0.201	–0.217	0.176	0.960	12.402	0.382	–0.350	0.048	0.936	12.715
Flap up	0.109	0.439	0.215	–0.872	6.986	1.441	0.188	–0.012	–0.982	5.791

The distal end of forelimb was composed of three main bones (ulna, radius and carpometacarpus) and two small bones (ulnare and radiale). The relationship of the three main bones and two small bones formed four subjoints to construct the wrist joint. Considering that only three sub-joints were independent, therefore, ulna–carpometacarpus joint, ulna–ulnare joint, radius–radiale joints were discussed to study the wrist joint behaviors. The radius–carpometacarpus joint motion can be deduced with the five bones. During the quantitively analysis, the extended posture was identified as the reference frame, parent bones of all the other eight postures were moved to the same position at first, as shown in Figs. 4(d)–4(f). Thereafter, motions (both translations and rotations) of child bone relative to the parent bone were calculated to obtain relative displacement, rotating axes and rotating angles as listed in Table 3.

Table 3. Relative motion of the wrist joint.

Posture	Ulnare relative to ulna					Radiale relative to radius					Carpometacarpus relative to ulna				
	T (mm)		A		θ (°)	T (mm)		A		θ (°)	T (mm)		A		θ (°)
Half flexion	0.762	–0.690	0.668	–0.278	14.688	0.968	0.507	0.546	–0.667	15.245	1.650	–0.330	0.170	–0.929	23.456
Flexion	1.904	–0.894	0.427	–0.137	30.248	1.849	–0.636	–0.173	–0.752	37.729	2.962	–0.254	0.094	–0.963	55.252
Small torsion	0.283	0.193	0.980	–0.041	5.261	0.989	0.646	0.569	–0.510	10.131	1.401	0.138	0.524	–0.841	10.919
Large torsion	0.327	–0.320	0.907	0.275	8.683	1.582	0.491	0.815	–0.308	13.357	1.679	0.448	0.468	–0.762	10.468
Small deep stall	0.269	0.244	–0.210	0.947	7.701	1.322	0.604	0.666	–0.437	11.033	0.588	0.251	–0.374	0.893	5.682
Large deep stall	0.455	–0.734	0.603	–0.315	4.107	0.696	0.545	0.650	–0.529	11.332	1.230	–0.099	–0.877	0.471	2.483
Flap down	0.226	–0.402	0.162	–0.901	4.637	1.328	–0.252	0.178	–0.951	10.052	0.364	–0.755	–0.308	–0.579	5.301
Flap up	0.526	0.892	–0.449	0.056	4.166	2.448	0.630	0.725	0.278	9.430	0.329	0.890	0.455	–0.038	4.038

It is shown that translations of ulnare relative to ulna were all within 1 mm, except for the flexed posture. On the other hand, more larger translations were observed for the radiale. In all the cases, the maximum rotating angle appeared in the flexion posture followed with the half flexion value which was nearly half the rotating angle of the flexion posture. Unfortunately, the rotating axes of ulnare, radiale and carpometacarpus varied with each other, which implied a three-dimensional transformation during the simple wing extending/folding motion. Besides, the rotating angle declined to a small value in the other postures, especially in the ulnare motion, and two rotational DOFs, flexion and torsion, were estimated for the carpometacarpus. The measured motions of the 7 joints are shown in Fig. 5.

During the measurement, each posture was used to compare with the extended one, leading to eight residuals of each bone in all the cases. Thus, in order to provide a reference residual value for the following skeleton optimization, the posture mean residual was defined as

$$f(i) = \frac{\sum_{j=2}^{9} f(j,i)}{8}, \tag{4}$$

where $f(i)$ was the mean residual of bone i of all the postures, $f(j,i)$ was the residual of bone i between the moved extended posture ($j = 1$) and the jth initial posture which was calculated using Eq. (3). The mean residual of each bone is listed in Table 4.

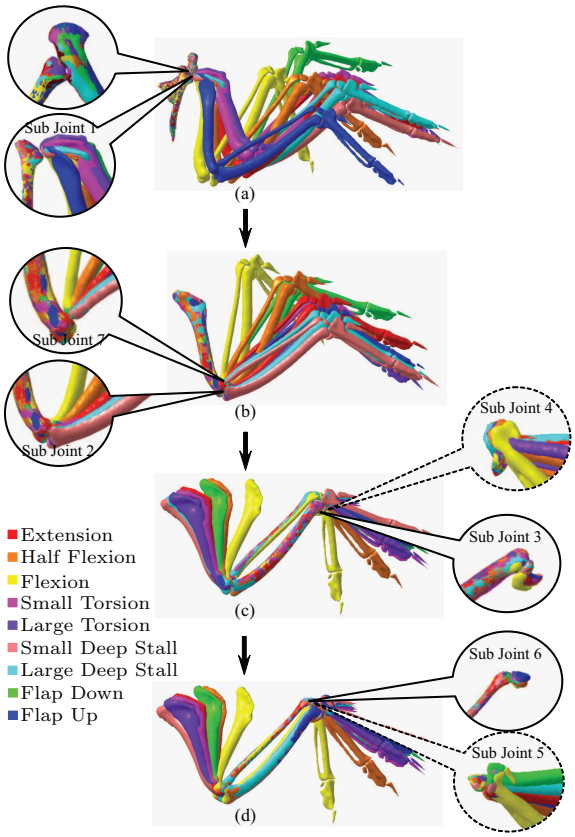


Fig. 5. Illustration of the scanned wing skeletons' transformation to each bone at extension status using the proposed optimization method: (a) transform to scapulae to study shoulder joint; (b) transform to humerus to study elbow joint; (c)–(d) transform to ulna and radius to study wrist joint.

Table 4. The mean residual of each bone.

Bone	Humerus	Ulna	Ulnare	Carpometacarpus	Radiale	Radius
Residual (mm)	0.5232	0.4970	0.2452	0.5194	0.2834	0.4944

4. Optimization of wing skeleton model

4.1. Optimization method

To obtain a closed-loop mechanism that can represent the elbow-wrist coupling motion in all the wing motions, a six-bar model of the wing skeleton including the two wrist bones (ulnare and radiale) and four main wing bones (humerus, ulna, carpometacarpus and radius) was proposed. However, different joint type between neighboring bones usually leaded to different fitting precision, and there was no doubt that spherical joints give rise to a high fidelity. The question was how can the six-bar model achieves a high fidelity while reduces the independent DOFs. Three types of joints (revolute joint with 1 DOF, universal joint with 2 DOFs, spherical joint with 3 DOFs) were used to find out the optimized relationship between neighboring bones.

The brachium area includes the motion of shoulder joint (sub-joint 1). It has been proved that there is no relative motion between the coracoid and the scapula in Subsection 3.2. Therefore, the scapula was used instead of the body, in order to simplify it into a multi-bar motion with one single joint. The antebrachium was simplified as a six-bar closed-loop model composed of six bones (humerus, ulna, ulnare, carpometacarpus, radiale and radius) and six joints (sub joint 2 to sub joint 7). Therefore, the whole wing skeleton consisted of sub joints ranging from 1 to 7. Above all, sub joints ranging from 2 to 7 formed a closed-loop model, and the DOFs of sub-joint 1 were independent of the closed-loop model. In the optimization calculation of six-bar closed-loop model, the humerus was considered as a fixed bar.

The following global optimization equation, using the GlobalSearch method in MATLAB software, was used to find the minimum residual:

$$g(q) = \min(d), \tag{5}$$

where d was the mean bones residual of all postures. It should be noted that only the residuals of ulna, radius and carpometacarpus were used in the mean value calculations. It was reasonable because ulnare and radiale were quite small with little features which was difficult to identify, as a result, too many cloud points were used to construct their geometry shapes. Thus, there were 3 bone residuals that need to calculate in each posture in the six-bar closed-loop mechanism.

The optimization variable was $q = [\text{Center}_k, \text{Direction}_k, \text{Rotation}_k]$. Center_k and Direction_k were centre location and rotating axis of the kth joint, Rotation_k was the Euler angle. In fact, these optimization variables were not independent considering that each part of the multibody system was connected by kinds of joints. Joints were modeled by constraint equations, which are composed of location constraints and vector constraints. Assume a joint connects ith parent body and jth child body at point m and point n, respectively. Location constraints were constructed at point m and point n, while the z axis of one joint parallels to the other as shown in Fig. 6. The location constraint equations were

$$r_{im} - r_{jn} = 0, \tag{6}$$

where r_{im} and r_{jn} were locations of point m and point n respectively under the global coordinate. The vector constraint equations were constructed to meet the relative angular requirements of the two bodies as

$$v_m^x v_n^z = 0. \tag{7}$$

The equations of fixed joint were

$$C_{\text{fixed}} = \begin{bmatrix} r_{im} - r_{jn} = 0 \\ v_m^x v_n^z = 0 \\ v_m^y v_n^z = 0 \\ v_m^y v_n^x = 0 \end{bmatrix}. \tag{8}$$

Joints with motion control were developed in order to merge the joint into the optimization method. The equations of controlled revolute joint were

$$C_{\text{revolute}} = \begin{bmatrix} r_{im} - r_{jn} = 0 \\ v_m^x v_n^z = 0 \\ v_m^y v_n^z = 0 \\ v_m^y v_n^x = \sin(\alpha t) \end{bmatrix}. \tag{9}$$

The equations of controlled universal joint were

$$C_{\text{universal}} = \begin{bmatrix} r_{im} - r_{jn} = 0 \\ v_m^x v_n^z = \sin(\alpha t) \\ v_m^y v_n^z = \sin(\beta t) \\ v_m^y v_n^x = 0 \end{bmatrix}. \tag{10}$$

The equations of controlled spherical joint were

$$C_{\text{spiral}} = \begin{bmatrix} r_{im} - r_{jn} = 0 \\ v_m^x v_n^z = \sin(\alpha t) \\ v_m^y v_n^z = \sin(\beta t) \\ v_m^y v_n^x = \sin(\gamma t) \end{bmatrix}. \tag{11}$$

Here α, β, γ were the rotational angles extracted from Rotation_k.

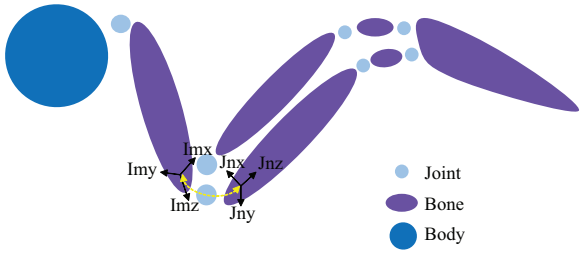


Fig. 6. Joint connection.

4.2. Results and discussion

Since spherical joint enables a child bone revolute around the parent bone in all directions, thus, it was used in all the sub joints. The use of spherical joint provided the six-bar model with more DOFs but made the six-bar model difficult to control. Fortunately, it was found that some child bone only rotated around the parent bone in limited directions based on the

relative motion discussed in Subsection 3.2. Thus, universal joint type (2 DOFs) was used in all joints except the shoulder joint, and revolute joint type was used in ulna–ulnare and radiale–radius types. We hope that the wing morphing motions can be reconstructed with the least DOFs. The possible joint types that meet the kinematic law of each joint are preliminarily selected, as shown in Table 5.

Table 5. Joint types optimized in the six-bar model.

Joint number	Two bones adjacent to a joint	Joint types
1	scapula–humerus	spherical
2	humerus–ulna	spherical, universal
3	ulna–ulnare	spherical, universal, revolute
4	ulnare–carpometacarpus	spherical, universal
5	carpometacarpus–radiale	spherical, universal
6	radiale–radius	spherical, universal, revolute
7	radius–humerus	spherical, universal

Since the shoulder joint was simplified as a spherical joint which was independent of the other joint rotations, thus the remained closed-loop skeleton model antebrachium with joints ranging from 2 to 7 would be optimized. Elbow and wrist joints enabled the six bars with a closed-loop mechanism. Thus, it was convenient to optimize the joint types of the six-bar model by transforming all the humeri to the same position, as shown in Fig. 5(b). Note that when calculating the DOFs of the six-bar closed-loop model, the humerus was considered as a fixed bar, and there were five moving bars: ulna, ulnare, carpometacarpus, radiale and radius. Additionally, there were $2^4 \times 3^2 = 144$ cases needed to optimized, which were divided into nine groups according to the DOFs of the mechanism. The calculated residuals are shown in Fig. 7.

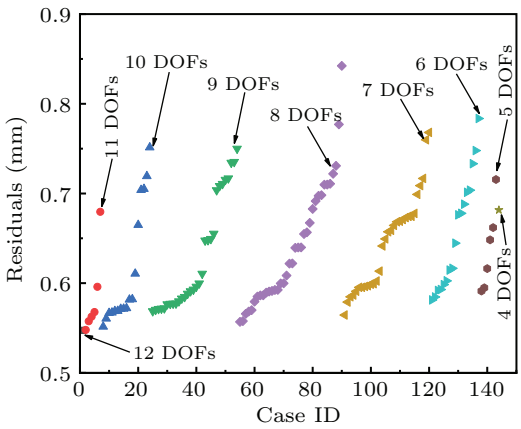


Fig. 7. Optimized residuals of the six-bar mechanism with joints range from 2 to 7.

Table 6. Cases with the smallest residuals of each DOFs group: spherical joint represented by S, universal joint represented by U, revolute joint represented by R.

DOFs	Case number	Joint ID						Residual (mm)
		Joint 2	Joint 3	Joint 4	Joint 5	Joint 6	Joint 7	
12	1	S	S	S	S	S	S	0.5474
	2	S	S	U	S	S	S	0.5478
11	3	S	S	S	S	S	U	0.5575
	4	S	S	S	S	U	S	0.5626
	5	S	S	U	U	S	S	0.5514
10	6	S	S	U	S	S	U	0.5605
	7	S	U	S	U	S	S	0.5667
	8	S	S	U	U	U	S	0.5688
9	9	S	U	S	S	R	S	0.5717
	10	S	U	U	S	S	U	0.5720
	11	S	S	U	S	R	U	0.5568
8	12	S	R	S	S	U	U	0.5577
	13	S	R	U	S	U	S	0.5658
	14	S	R	U	S	U	U	0.5644
7	15	S	R	U	S	R	S	0.5790
	16	S	R	U	U	S	U	0.5848
	17	S	U	U	U	R	U	0.5813
6	18	S	R	U	U	R	S	0.5846
	19	U	U	U	U	R	S	0.5918
	20	U	R	U	S	R	U	0.5912
5	21	U	R	U	U	R	S	0.5948
	22	U	U	U	U	R	U	0.6162
4	23	U	R	U	U	R	U	0.6816

As we expected, a minimum residual of 0.547 was obtained in the all-spherical joint case since spherical joint enabled a bone rotate in all direction. However, 12 DOFs of the mechanism made it difficult to control. Besides, existence of non-zero residual implied that both rotation and translation should be included in the nature bird joint motion investigations, which also made it difficult to fabricate. 23 cases with the smallest residuals in each group were detailly listed in Table 6. It was shown that the maximum value existed in the DOFs 4 group. A simple six-bar model with a high recon-

struct fidelity will be convenient to illustrate the wing morphing mechanism. There are two principles when selecting the joint types: (1) make the residuals of the mechanism as small as possible so that the model can reconstruct bird motion as accurately as possible; (2) reduce the redundant DOFs of the mechanism as much as possible. As a result, the U–R–U–S–R–U case was personally recommended for it can reconstruct the wing morphing motions with a high precision but only 5 DOFs, as shown in Fig. 8.

It was shown that all the optimized residual listed was under 0.59 when a spherical joint was used for sub joint 2, which implied joint type of sub joint 2 had non-negligible effect on the optimized residual. The relative motions between radius and radiale as well as the one between ulna and ulnare were small, a revolute joint with one DOF was sufficient to approximate their rotations. On the contrary, one or more spherical joints were usually adopted to adjust the relative rotations among wrist and the carpometacarpus bones, which were mainly caused by the folding/extending and flapping motions. The recommended U–R–U–S–R–U model could reconstruct almost all the wing motions with a small residual of 0.5912 mm, as shown in Fig. 9. Bones calculated using the six-bar model illustrated with red color were compared with the scanned bones. Above all, it was shown that all the bones fitted well with each other using the proposed six-bar model.

In addition, the humerus was connected to the body using a spherical joint with 3 DOFs, as shown in Fig. 8 (sub joint 1). Finally, the proposed six-bar closed-loop model with seven joints of S–U–R–U–S–R–U has six moving bars and 8 DOFs.

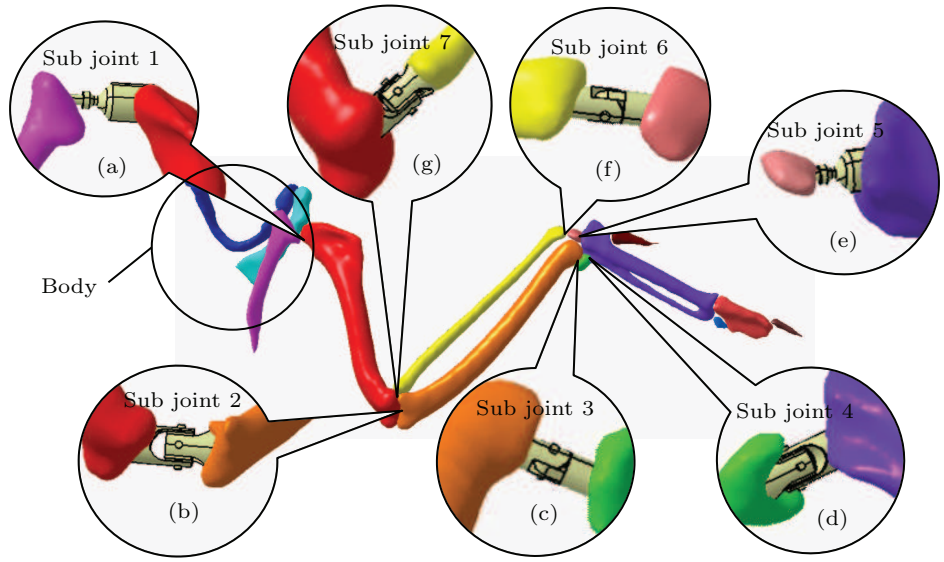


Fig. 8. Obtained six-bar model with seven joints: (a) spherical joint; (b) universal joint; (c) revolute joint; (d) universal joint; (e) spherical joint; (f) revolute joint; (g) universal joint.

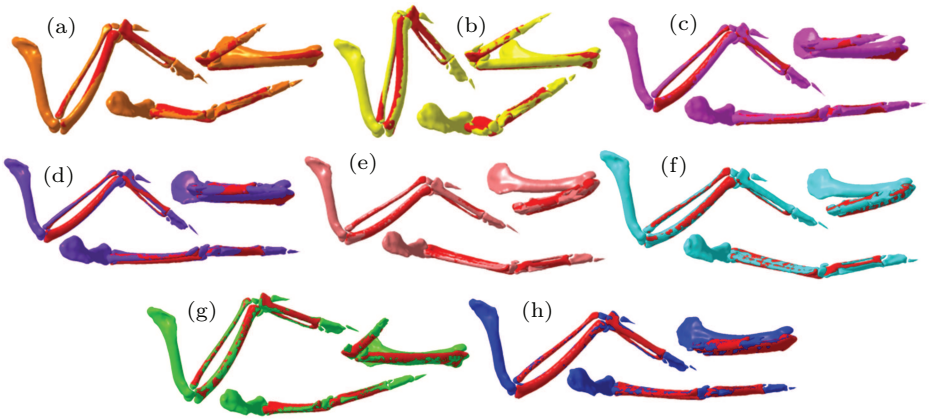


Fig. 9. Comparison of the morphing shapes between the scanned bones of a falcon and the six-bar model in case 20: (a) half flexion; (b) flexion; (c) small torsion; (d) large torsion; (e) small deep stall; (f) large deep stall; (g) flap down; (h) flap up.

5. Conclusion

Falco peregrinus is one of the world's fastest birds and investigation of the wing forelimb structure would be well suited for future studies about avian flights with excellent morphing abilities. However, wing motion database of *Falco peregrinus* was nonexistent yet. In order to fill this gap, the morphing wing mechanism was quantitatively analyzed.

1. Nine critical postures of *Falco peregrinus* were examined and CT scans were performed on the *Falco peregri-*

nus to obtain its wing skeleton shapes with different postures. Thereafter, an optimization algorithm was proposed to measure relative motion of each bone. Translations, rotating axes and angles of shoulder joint, elbow joint, and wrist joint were all quantitatively measured to enrich the wing motion database of *Falco peregrinus*. We think that the established motion data base will be essential for understanding avian flight.

2. A six-bar model of the wing skeleton including the two wrist bones and four main wing bones was proposed using the obtained wing motion database. It was interesting that how the wing joints worked to connecting neighboring bones to constitute a wing skeleton. Thereafter, an optimization algorithm was developed to optimize the joint types based on the multibody dynamics theory. There was no doubt that all spherical-joint model gives rise to the highest fidelity, however, it was difficult to control. As a result, the six-bar model of S–U–R–U–S–R–U with 8 DOFs was recommended for wing motion study because that it can reconstruct the wing morphing motions with a high precision. It is implied that muscles or tendons restricted the wing motion even a bird died, which should be investigated in the future work.

Acknowledgements

The authors would like to thank the team of Zhongyong Fan for all their contributions on the specimen, thank the team of Yahui Cui for CT scans, thank the team of Dawei Liu for the mechanical design. The work at ZJUT was supported by the National Natural Science Foundation of China (Grant Nos. 52175279, 52075489, and 51705459) and the Natural Science Foundation of Zhejiang Province, China (Grant Nos. LY20E050022 and LGG20E050017).

References

[1] Harvey C, Baliga V B, Lavoie P and Altshuler D L 2019 *J. R. Soc. Interface* **16** 20180641
[2] Cheney J A, Stevenson J P J, Durston N E, Maeda M, Song J L, Megson-Smith D A, Windsor S P, Usherwood J R and Bomphrey R J 2021 *J. R. Soc. Interface* **18** 20210349
[3] Tang D, Liu D W, Yang Y, Li Y, Huang X P and Liu K 2021 *Chin. Phys. B* **30** 034701
[4] Tang D, Liu D W, Zhu H, Huang X P, Fan Z Y and Lei M X 2020 *Chin. Phys. B* **29** 024703
[5] Harvey C, Baliga V B, Wong J C M, Altshuler D L and Inman D J 2022 *Nature* **603** 648
[6] Lentink D, Müller U K, van Gestel W, van Leeuwen J L, Stamhuis E J, Videler J J, de Kat R, Veldhuis L L M, Henningsson P and Hedenström A 2007 *Nature* **146** 1082
[7] Sullivan T N, Meyers M A and Arzt E 2019 *Science Advances* **5** eaat4269
[8] Shatkovska O V and Ghazali M 2017 *European Zoological Journal* **84** 390
[9] Liu T S, Kuykendoll K, Rhew R and Jones S 2006 *AIAA Journal* **44** 954
[10] Gillies J A, Thomas A L R and Taylor G K 2011 *Journal of Avian Biology* **42** 377
[11] Mills R, Hildenbrandt H, Taylor G K and Hemelrijk C K 2018 *PLOS Computational Biology* **14** e1006044
[12] Halsey L G, Portugal S J, Smith J A, Murn C P and Wilson R P 2009 *Journal of Field Ornithology* **80** 171
[13] Franklin D C 1999 *Biological Conservation* **90** 53
[14] Tucker V A 1998 *Journal of Experimental Biology* **201** 403
[15] Ponitz B, Schmitz A, Fischer D, Bleckmann H and Brucker C 2014 *PLOS one* **9** e86506
[16] Bergmann C 1839 *Arch. Anat. Physiol. wiss Med.* **6** 296
[17] Ashley M. H, Jeffery W R and John R H 2018 *Frontiers in Bioengineering and Biotechnology* **6** 140
[18] Tang D, Liu D W and Fan Z Y 2020 *Journal of Testing and Evaluation* **48** 20190475
[19] Fisher H I 1957 *Science* **126** 446
[20] Beaufrere H, Ammersbach M, Nevarez J, Heggem B and Tully T N 2012 *Journal of Avian Medicine and Surgery* **26** 94
[21] Rupiper D J and Ramsay E 1993 *J. Assoc. Avian Vet.* **7** 160
[22] Vazquez R J 1994 *Zoomorphology* **114** 59
[23] Baier D B, Gatesy S M and Jenkins F A 2007 *Nature* **445** 307
[24] Meyers R A and Stakebake E F 2005 *Journal of Morphology* **263** 12
[25] Stowers A K, Matloff L Y and Lentink D 2017 *J. R. Soc. Interface* **14** 20170224
[26] Pennycuick C J 2008 *Theoretical Ecology Series* **5** 409
[27] Parslew B 2015 *J. R. Soc. Interface* **12** 20140953
[28] Hedrick T L, Tobalske B W, Ros I G, Warrick D R and Biewener A A 2012 *Proc. Roy. Soc. B: Biolog. Sci.* **279** 1986
[29] Parslew B and Crowther W J 2010 *Journal of Biomechanics* **43** 3191
[30] Vazquez R J 1992 *Journal of Morphology* **211** 259
[31] Bin Abas M F, Rafie A S B, Bin Yusoff H and Bin Ahmad K A 2016 *Chinese Journal of Aeronautics* **29** 1159
[32] Phan H V and Park H C 2019 *Progress in Aerospace Sciences* **111** 100573
[33] He W, Mu X X, Zhang L and Zou Y 2021 *IEEECAA Journal of Automatica Sinica* **8** 148
[34] Burgess S 2021 *Bioinspiration & Biomimetics* **16** 041001
[35] Conn A T, Burgess S C and Ling C S 2007 *Proceedings of the Institution of Mechanical Engineers, Part C: Journal of Mechanical Engineering Science* **221** 1211
[36] Tsai B J and Fu Y C 2009 *Aerospace Science and Technology* **13** 383
[37] Zhang Z Q, Zhang Y, Zhao J and Zhou Z Y 2022 *Mechanism and Machine Theory* **170** 104730
[38] Rajabi H, Ghoroubi N, Stamm K, Appel E and Gorb S N 2017 *Acta Biomaterialia* **60** 330
[39] Tang D, Huang X P, Che J Q, Jin W J, Cui Y H, Chen Y J,Yuan Y J, Fan Z Y, Liu W W, Wang S Y, Yang Y and Liu D W 2022 *Fundamental Research*